

Spin-valley physics in anomalous thermoelectric responses of the spin-orbit coupled α - T_3 system with broken time-reversal symmetry

Lakpa Tamang and Tutul Biswas

*Department of Physics, University of North Bengal, Raja Rammohunpur, Darjeeling-734013, India**

(Dated: March 17, 2026)

We extract spin-valley physics in the anomalous Hall and Nernst responses of the α - T_3 system, considering the simultaneous presence of the Kane–Mele type intrinsic spin–orbit interaction (SOI) and a time-reversal symmetry breaking staggered magnetization. Within a full low-energy continuum model, we compute the spin- and valley-resolved anomalous Hall, and anomalous Nernst conductivities. We show that the interplay between the SOI, magnetization, and a model parameter α for the α - T_3 lattice enables efficient tuning of spin- and valley-dependent Hall and Nernst signals. The spin-valley physics of the Hall and Nernst responses in the absence and presence of the magnetization are well explained. The peak-dip features of the Nernst responses are also understood from the corresponding Hall responses through the Mott relation. We find that the magnetization introduces highly tunable spin and valley polarizations, which are calculated from the spin- and valley-resolved Nernst conductivities. It is shown that both the spin and valley polarizations can attain nearly complete polarization over extended regions of the parameter space. Overall, our results highlight the α - T_3 lattice as a promising platform for spin and valley caloritronic applications.

I. INTRODUCTION

The generation and control of spin-polarized currents constitute a solid foundation of modern spintronics. Spintronics, which exploits the intrinsic spin of electrons in addition to their charge, has emerged as a promising avenue for the realization of energy-efficient and multifunctional devices [1–5]. Over the years, considerable effort has been devoted into developing efficient mechanisms for producing spin-polarized currents. These include electrical injection through ferromagnets [6, 7], the spin Hall effect [8–10], spin injection [11–13], voltage controllable generator [14], and various spin pumping schemes [15–22].

A closely related research direction, spin caloritronics [23, 24], explores the generation and control of spin currents through thermal gradients rather than applied electric fields. A central advance in this field is the observation of the spin Seebeck effect [25–29], which demonstrates that a temperature gradient can be used as an efficient tool to generate spin current. Analogously, valley caloritronics [30] combines thermoelectric transport with the valley degree of freedom emerging from two inequivalent valleys in the low-energy band structure of Dirac materials such as graphene [31–33], silicene [34], transition-metal dichalcogenides [35, 36], etc. Electronic states near these valleys act as distinct pseudospin flavors, enabling their selective manipulation via external fields or symmetry-breaking perturbations.

The emergence of nontrivial Berry curvature in such materials due to some broken symmetries has attracted significant attention, leading to extensive studies of unconventional transport phenomena, including the anomalous Hall and Nernst effects, their spin and valley analogues, as well as the thermal Hall responses [37–43]. Experimental demonstrations of these ef-

fects [44–50] further underscore their technological relevance. In particular, Nernst responses have played a pivotal role in identifying vortex phases in type-II superconductors [45, 46], probing topological surface states [42], and enabling the generation of pure spin and valley currents [39].

Motivated by these developments, we focus on Berry curvature-mediated spin and valley transport in the α - T_3 system [51], a two-dimensional (2D) lattice model that serves as a link between graphene and dice lattice [52–54] through the smooth tuning of the parameter α between 0 and 1. Within nearest-neighbor tight-binding approximation, the low-energy spectrum of such a system possesses two inequivalent Dirac valleys K and K' . Each valley consists of a pair of linearly dispersive spin degenerate bands accompanied by a dispersionless flat band at zero energy. Interestingly, the Berry phase corresponding to the α - T_3 system depends on α , which gives rise to a broad range of unusual phenomena [55–73]. Experimental routes to realizing α - T_3 physics have been proposed in semiconductor heterostructures and cold-atom optical lattices [74, 75]. In particular, $\text{Hg}_{1-x}\text{Cd}_x\text{Te}$ heterostructure at critical doping ($x = 0.17$) has been demonstrated theoretically to mimic an α - T_3 system with $\alpha = 1/\sqrt{3}$ [76]. In a series of recent works [77–81], it has been explicitly shown that an off-resonant circular polarized radiation can induce topological phases into the α - T_3 model. Notably, the irradiated system exhibits a topological phase transition (TPT) across $\alpha = 1/\sqrt{2}$, characterized by a quantized jump in the Chern number from $C = 1$ to $C = 2$.

The incorporation of next-nearest-neighbor hoppings in the tight-binding Hamiltonian gives rise to intrinsic spin-orbit interaction (SOI) of Kane–Mele type [82, 83], enabling the emergence quantum spin-Hall (QSH) phases in the α - T_3 model. Moreover, the system undergoes a TPT across $\alpha = 1/2$, accompanied by a change in the spin Chern number from $C_s = 1$ to $C_s = 2$ [84]. In a recent study [85], the signatures of such a TPT have been identified in the orbital magnetization and circular dichroism. However, the symmetries of the underlying system impose severe constraints on the experi-

*Electronic address: tbiswas@nbu.ac.in

mental observation of such effects. Introducing a staggered sublattice magnetization M , which breaks the time-reversal symmetry, lifts these restrictions [85]. The interplay between M and α also generates a rich phase diagram characterized by distinct combinations of C and C_s [84].

The thermoelectric properties of α - T_3 systems, both in the presence and absence of a magnetic field have been investigated in the recent past [71–73]; however, the role of SOI has remained largely overlooked. To address this gap, here we investigate the anomalous thermoelectric response of the α - T_3 system in the presence of intrinsic Kane-Mele type SOI. More specifically, we perform a detailed analysis of spin and valley Hall and Nernst effects in the spin-orbit coupled α - T_3 system, both in the presence and absence of a staggered sublattice magnetization. Using a low-energy Kane-Mele-type model, we compute the Berry curvature and entropy-weighted transport coefficients. We show that the interplay of various parameters such as chemical potential, SOI strength, magnetization, and α enables precise control over spin- and valley-polarized thermoelectric responses. It is also demonstrated that the Nernst response of the α - T_3 system produces tunable spin and valley polarizations, exhibit rich structures, featuring extended regions of nearly complete polarization.

The rest of the paper is organized as follows. In Sec. II, we briefly introduce the essential features of the low-energy bandstructure of the α - T_3 system, incorporating the intrinsic Kane-Mele SOI term and a staggered magnetization. Section III presents the formalism for Berry curvature driven anomalous thermoelectric transport focusing on the spin- and valley-resolved Hall and Nernst conductivities. In Sec. IV, we provide a detailed numerical analysis of the band dispersions, Berry curvature distributions, and the associated Hall and Nernst responses, as well as the spin and valley polarization, both in the presence and absence of the magnetization. Finally, Sec. V summarizes our main findings.

II. LOW-ENERGY DESCRIPTION OF THE SPIN-ORBIT COUPLED α - T_3 SYSTEM

We begin by briefly describing the spin-orbit coupled α - T_3 lattice, considering the next-nearest-neighbor (NNN) interactions. The inclusion of NNN hopping introduces Kane-Mele type SOI [82]. As schematically illustrated in Fig. 1, a NNN hopping path comprises two consecutive nearest-neighbor (NN) segments, which may be traversed either clockwise or counterclockwise when viewed from the above along the direction perpendicular to the lattice plane. For instance, an electron can hop from a given B site to one of its NNN B sites either through an intermediate A or C site. There are four distinct NNN hopping channels: (i) A - B - A , (ii) B - A - B , (iii) B - C - B , and (iv) C - B - C . The first two pathways [(i) and (ii)] give rise to SOI of strength λ , while the latter two [(iii) and (iv)] contribute an SOI of strength $\alpha\lambda$. This scaling is consistent with the basic assumption of the α - T_3 model, wherein the NN hopping amplitude between B and C sites is α times of that between A and B sites. The A - C - A NNN process is

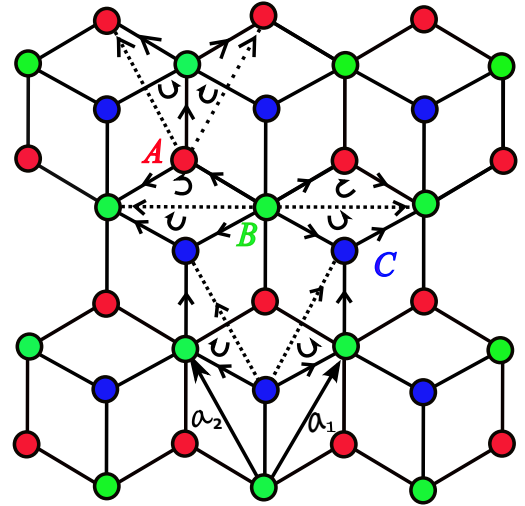


FIG. 1: (Color online) Schematic illustration of the α - T_3 lattice with hub (B) and rim (A , C) sites. The NN (NNN) hopping paths are indicated by solid (dashed) lines. The NN B - C hopping amplitude is α times to that of A - B hopping strength. The lattice translational vectors are $\mathbf{a}_1 = (\frac{\sqrt{3}}{2}, \frac{3}{2})a$ and $\mathbf{a}_2 = (-\frac{\sqrt{3}}{2}, \frac{3}{2})a$, where a is the NN distance.

neglected, following the same logic that the α - T_3 model excludes any direct A - C NN coupling.

By incorporating both NN and NNN hopping terms, the low-energy tight-binding Hamiltonian in momentum space for a given spin index σ and valley index η can be expressed as [84, 85]

$$H_{\sigma}^{\eta}(\mathbf{k}) = \lambda\eta\sigma \begin{pmatrix} -\cos\phi & f_{\mathbf{k}}\cos\phi & 0 \\ f_{\mathbf{k}}^*\cos\phi & \cos\phi - \sin\phi & f_{\mathbf{k}}\sin\phi \\ 0 & f_{\mathbf{k}}^*\sin\phi & \sin\phi \end{pmatrix}, \quad (1)$$

where $\phi = \arctan(\alpha)$ and $f_{\mathbf{k}} = \sigma\hbar v_F(k_x + i\eta k_y)/\lambda$, with v_F denoting the Fermi velocity. The diagonal elements in the Hamiltonian indicate that the SOI induces an α -dependent mass term in the energy spectrum.

To incorporate the effect of staggered magnetization, we consider a simple A - C sublattice configuration, where magnetization takes opposite signs on the A and C sites and vanishes on the B sites. It is important to note that this A - C staggered configuration is specific to the α - T_3 lattice with $\alpha \neq 0$. In the graphene limit ($\alpha = 0$), the C sublattice is absent, and the lattice reduces to the standard honeycomb structure consisting only of A and B sublattices. Consequently, for $\alpha = 0$ one must instead consider staggered magnetization between the A and B sublattices. Thus, we adopt an A - C staggered configuration for $\alpha \neq 0$, and an A - B staggered configuration in the graphene limit.

Therefore, for $\alpha \neq 0$, the staggered magnetization term added

to the Hamiltonian in Eq. (1) reads as

$$H_M = M\sigma s^z = M\sigma \begin{pmatrix} 1 & 0 & 0 \\ 0 & 0 & 0 \\ 0 & 0 & -1 \end{pmatrix}, \quad (2)$$

where s^z represents the z -component of the pseudospin-1 operator associated with the lattice. The presence H_M explicitly breaks the time-reversal symmetry (TRS) of the Hamiltonian.

The energy spectrum is then obtained as

$$\varepsilon_{\eta,\sigma}^n(\mathbf{k}) = 2\sqrt{\frac{-p}{3}} \cos\left[\frac{1}{3} \arccos\left(\frac{3q}{2p}\sqrt{\frac{-3}{p}}\right) - \frac{2\pi n}{3}\right], \quad (3)$$

with

$$p = \frac{1}{2}\lambda^2 \sin(2\phi) + \sqrt{2}\lambda M\eta \sin\left(\phi + \frac{\pi}{4}\right) - (\lambda^2 + \hbar^2 v_F^2 k^2 + M^2), \quad (4)$$

and

$$q = \frac{1}{\sqrt{2}}\lambda\sigma\eta \sin(2\phi) \cos\left(\phi + \frac{\pi}{4}\right) (\lambda^2 + \hbar^2 v_F^2 k^2) + \sqrt{2}\lambda\sigma\eta \cos\left(\phi + \frac{\pi}{4}\right) M^2 - M\sigma \cos(2\phi) (\lambda^2 + \hbar^2 v_F^2 k^2). \quad (5)$$

The corresponding eigenfunction is expressed as

$$\psi_{\eta,\sigma}^n(\mathbf{k}) = \frac{1}{\sqrt{1 + |F_{\mathbf{k}}|^2 + |G_{\mathbf{k}}|^2}} \begin{pmatrix} F_{\mathbf{k}} \\ 1 \\ G_{\mathbf{k}} \end{pmatrix} \frac{e^{i\mathbf{k}\cdot\mathbf{r}}}{\sqrt{S}}, \quad (6)$$

where $F_{\mathbf{k}} = f_{\mathbf{k}} \cos\phi / (\tilde{\varepsilon}_{\eta,\sigma}^n + \cos\phi)$ and $G_{\mathbf{k}} = f_{\mathbf{k}}^* \sin\phi / (\tilde{\varepsilon}_{\eta,\sigma}^n - \sin\phi)$ with $\tilde{\varepsilon}_{\eta,\sigma}^n = \varepsilon_{\eta,\sigma}^n / (\eta\sigma\lambda)$. Here, S is the area of the sample.

The quantity n in Eqs. (3) and (6) denotes the band index, with $n = 0, 1, 2$ corresponding to the conduction band (CB), flat band (FB), and valence band (VB), respectively. In the absence of M , the TRS is preserved for all α , whereas the inversion symmetry (IS) is broken for $0 < \alpha < 1$. Therefore, in the limiting cases $\alpha = 0$ (graphene) and $\alpha = 1$ (dice lattice), both the TRS and IS are simultaneously present, resulting in spin and valley degenerate energy bands. However, the presence of the staggered magnetization lifts only the valley degeneracy of the energy bands in these two limiting cases. Nevertheless, for intermediate values of α , both the spin and valley degeneracies are lifted due to the simultaneous breaking of IS and TRS. For $\alpha = 1$, the expression for the energy eigenvalue simplifies to

$$\varepsilon^d = (\hbar^2 v_F^2 k^2 + \Delta_d^2)^{1/2} \quad (7)$$

where, and similarly, for $\alpha = 0$ the energy eigenvalue can be expressed as

$$\varepsilon^g = (\hbar^2 v_F^2 k^2 + \Delta_g^2)^{1/2} \quad (8)$$

with $\Delta_g = (\lambda\eta\sigma - M\sigma)$.

III. FORMALISM FOR THE BERRY CURVATURE MEDIATED ANOMALOUS THERMOELECTRIC TRANSPORT

We now turn to the spin- and valley-resolved anomalous Hall effect (AHE) and anomalous Nernst effect (ANE). The AHE (ANE) corresponds to the generation of a transverse electric voltage in response to a longitudinal electric field (temperature gradient). The central origin of both effects is the Berry curvature, which introduces an anomalous velocity correction to the semiclassical equations of motion.

For an electron in a given Bloch band (n, σ, η), the modified velocity in the presence of an external electric field reads

$$\mathbf{v}_{\eta,\sigma}^n(\mathbf{k}) = \frac{1}{\hbar} \nabla_{\mathbf{k}} \varepsilon_{\eta,\sigma}^n(\mathbf{k}) - \frac{e}{\hbar} \mathbf{E} \times \boldsymbol{\Omega}_{\eta,\sigma}^n(\mathbf{k}), \quad (9)$$

where

$$\boldsymbol{\Omega}_{\eta,\sigma}^n(\mathbf{k}) = \nabla_{\mathbf{k}} \times \langle u_{\eta,\sigma}^n(\mathbf{k}) | i \nabla_{\mathbf{k}} | u_{\eta,\sigma}^n(\mathbf{k}) \rangle \quad (10)$$

is the Berry curvature associated with the periodic part of the Bloch function $|u_{\eta,\sigma}^n(\mathbf{k})\rangle = |\psi_{\eta,\sigma}^n(\mathbf{k})\rangle e^{-i\mathbf{k}\cdot\mathbf{r}} \sqrt{S}$.

In a two-dimensional (2D) system confined to the xy plane, only the out-of-plane (z) component $\Omega_{\eta,\sigma}^n(\mathbf{k})$ of the Berry curvature contributes. Consequently, an electric field applied along x generates an anomalous transverse velocity along y , giving rise to the AHE. The symmetry properties of $\Omega_{\eta,\sigma}^n$ imply that a nonzero Berry curvature requires the breaking of either TRS or IS.

The spin- and valley-resolved anomalous Hall conductivity (AHC) and anomalous Nernst conductivity (ANC) are given, respectively, by

$$\sigma_{\text{H}}^{\eta,\sigma} = \frac{e^2}{\hbar} \int \frac{d^2\mathbf{k}}{(2\pi)^2} \sum_n f_{\eta,\sigma}^n(\mathbf{k}) \Omega_{\eta,\sigma}^n(\mathbf{k}), \quad (11)$$

and

$$\alpha_{\text{N}}^{\eta,\sigma} = -\frac{ek_B}{\hbar} \int \frac{d^2\mathbf{k}}{(2\pi)^2} \sum_n S_{\eta,\sigma}^n(\mathbf{k}) \Omega_{\eta,\sigma}^n(\mathbf{k}), \quad (12)$$

where the entropy density $S_{\eta,\sigma}^n$ is expressed as

$$S_{\eta,\sigma}^n = -f_{\eta,\sigma}^n \ln \left[\frac{f_{\eta,\sigma}^n}{1 - f_{\eta,\sigma}^n} \right] - \ln[1 - f_{\eta,\sigma}^n]. \quad (13)$$

Here, the function $f_{\eta,\sigma}^n(\mathbf{k}) = [e^{\beta(\varepsilon_{\eta,\sigma}^n - \mu)} + 1]^{-1}$ is usual Fermi-Dirac distribution with $\beta = 1/(k_B T)$ and μ as the chemical potential.

Unlike the AHC, which depends solely on the Berry curvature of filled bands, the ANC is a Fermi-surface property, sensitive both to the Berry curvature and entropy generation near the Fermi level. Because TRS enforces cancellation of the total (spin and valley summed) AHC and ANC for $M = 0$, we focus on their spin and valley components, defined as

$$\sigma_{\text{H}}^{\text{s}} = \sum_{\eta,\sigma} \sigma \sigma_{\text{H}}^{\eta,\sigma}, \quad \sigma_{\text{H}}^{\text{v}} = \sum_{\eta,\sigma} \eta \sigma_{\text{H}}^{\eta,\sigma}, \quad (14)$$

and

$$\alpha_N^s = \sum_{\eta,\sigma} \sigma \alpha_N^{\eta,\sigma}, \quad \alpha_N^v = \sum_{\eta,\sigma} \eta \alpha_N^{\eta,\sigma}. \quad (15)$$

Here, σ_H^s and σ_H^v denote spin Hall Conductivity (SHC) and valley Hall conductivity (VHC), respectively. In a similar way, α_N^s and α_N^v represent the spin Nernst conductivity (SNC) and valley Nernst conductivity (VNC), respectively.

For completeness, we introduce the spin- and valley-resolved polarization factors associated with the anomalous Nernst conductivity (ANC). These quantities provide a compact measure of the degree to which the transverse thermoelectric response originates from a single spin or valley channel. We define the spin (valley) polarization of the ANC as

$$P_{s(v)} = \frac{\left(|\alpha_N^{K\uparrow}| + |\alpha_N^{K'\uparrow(K\downarrow)}| \right) - \left(|\alpha_N^{K\downarrow(K'\uparrow)}| + |\alpha_N^{K'\downarrow}| \right)}{\left(|\alpha_N^{K\uparrow}| + |\alpha_N^{K'\uparrow}| + |\alpha_N^{K\downarrow}| + |\alpha_N^{K'\downarrow}| \right)}, \quad (16)$$

where $\alpha_N^{\eta,\sigma}$ denotes the ANC contribution from valley $\eta = \{K, K'\}$ and spin $\sigma = \{\uparrow, \downarrow\}$.

A value $P_{s(v)} = \pm 1$ indicates that the ANC originates entirely from a single spin (valley) channel, corresponding to a perfectly spin- or valley-polarized Nernst signal. Intermediate values $|P_{s(v)}| < 1$ quantify partial polarization arising from mixed spin or valley contributions, and $P_{s(v)} = 0$ signifies that the Nernst response arises from nearly symmetric contributions of opposite spins (valleys).

IV. RESULTS AND DISCUSSIONS

A. Band structure and Berry curvature

The low-energy band dispersions of the spin-orbit coupled α - T_3 lattice, both in the absence and presence of a staggered magnetization, are shown in Fig. 2. Figures 2(a) and 2(b) refer to the energy dispersions around the K and K' valleys, respectively, for $M = 0$, while Figs. 2(c) and 2(d) represent the same for $M = 50$ meV. The intrinsic SOI lifts the spin-degeneracy of the CB, FB, and VB by splitting them in their spin-up and spin-down counterparts. It also causes a distortion in the FB near the valley extremum. When $M = 0$, the role of the spin-up sub-bands in the K valley is interchanged by the spin-down sub-bands in the K' valley and vice versa i.e., $\varepsilon_{\uparrow}^K = \varepsilon_{\downarrow}^{K'}$ and $\varepsilon_{\downarrow}^K = \varepsilon_{\uparrow}^{K'}$, owing to the TRS.

When a finite staggered magnetization is introduced, the exact correspondence between the K and K' valleys is lost as a result of broken TRS, leading to a significant modification of the band structure. The interplay of the magnetization and SOI leads to an enhanced spin-splitting in the K' valley [Fig. 2(d)] relative to the K valley [Fig. 2(c)]. This asymmetry in the spin-splitting between the valleys has a pronounced effect on the thermoelectric response, as we will see later.

Using Eq. (10), we numerically calculate the Berry curvature for intermediate values of α both in the absence and presence

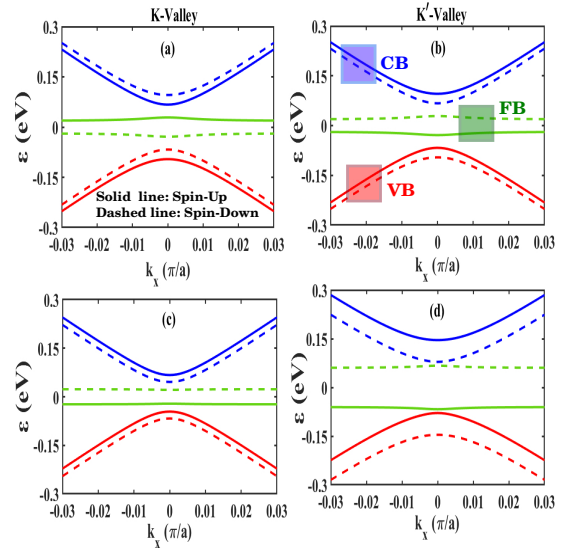


FIG. 2: (Color online) Low-energy dispersions in the K and K' valleys for $\alpha = 0.3$ and $\lambda = 100$ meV. Upper panels [(a) and (b)] represent $M = 0$, while lower panels [(c) and (d)] correspond to $M \neq 0$ case.

of the staggered magnetization. The distributions of the Berry curvature for both spin orientations ($\sigma = \uparrow, \downarrow$) in the K and K' valleys are depicted in Figs. 3 and 4, respectively. For both cases $M = 0$ and $M \neq 0$, the Berry curvatures of all spin-split sub-bands are predominantly concentrated near the Dirac points and exhibits clear spin-valley resolution. The FB acquires a finite yet spin-degenerate Berry curvature, satisfying $\Omega_{\eta,\sigma}^1(\mathbf{k}) = \Omega_{\eta,-\sigma}^1(\mathbf{k})$. However, the Berry curvatures associated with the CB and VB are spin-polarized, satisfying the relation: $\Omega_{\eta,\sigma}^0(\mathbf{k}) = \Omega_{\eta,-\sigma}^2(\mathbf{k})$.

In the absence of magnetization ($M = 0$), the Berry curvature obeys $\Omega_{\eta,\sigma}^n(\mathbf{k}) = -\Omega_{-\eta,-\sigma}^n(\mathbf{k})$, guaranteed by the TRS. This relation indicates that the total Berry curvature summed over the spin and valley degrees of freedom is zero, resulting in a vanishing net anomalous Hall response, despite significant local Berry curvature concentrated around the valleys.

The broken TRS for $M \neq 0$ leads to a significant redistribution and enhancement of the Berry curvature across all spin-split subbands. Specifically, the Berry curvatures associated with the CB and VB gain a dominant spin-dependent curvature near the valleys. The Berry curvature in the K' valley no longer mirrors that of the K valley, resulting in a finite imbalance between the spin channels. As a result, the spin and valley summed Berry curvature becomes nonzero, leading to a net anomalous Hall response. The pronounced contrast in Berry curvature patterns for different spin channels across both valleys highlights the tunability of spin and valley degrees of freedom via variation of the staggered magnetization.

Additionally, we obtain the following analytical expressions

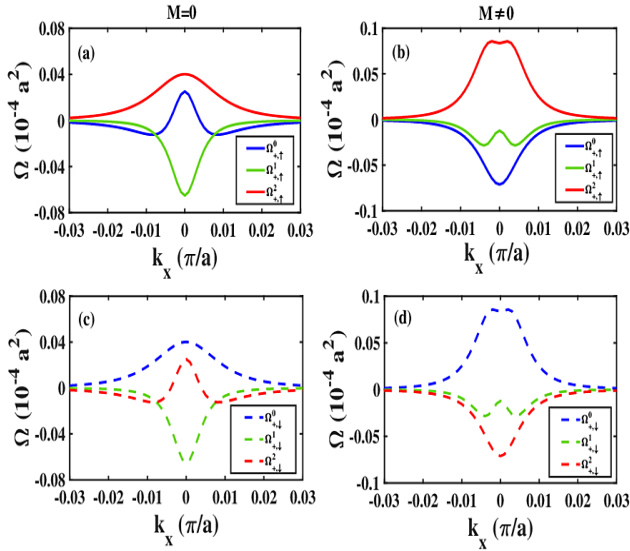


FIG. 3: (Color online) Berry curvature distribution $\Omega_{K,\sigma}^n(\mathbf{k})$ in the K valley for spin-up and spin-down bands. Left Panels [(a) and (c)] are for $M = 0$, while right panels [(b) and (d)] represents $M \neq 0$ case.

of the Berry curvature

$$\Omega_{\eta,\sigma}^n(\mathbf{k}) = \frac{\eta(n-1)\Delta_d\hbar^2v_F^2}{[\hbar^2v_F^2k^2 + \Delta_d^2]^{3/2}} \quad (17)$$

for $\alpha = 1$ and

$$\Omega_{\eta,\sigma}^n(\mathbf{k}) = \frac{\eta(n-1)\Delta_g\hbar^2v_F^2}{2[\hbar^2v_F^2k^2 + \Delta_g^2]^{3/2}} \quad (18)$$

for $\alpha = 0$. The index n takes only 0 and 2 in Eq. (18), representing the CB and VB of graphene, respectively. It is evident from Eqs. (17) and (18) that $\Omega_{\eta,\sigma}$ is both spin and valley resolved, as Δ_d and Δ_g are spin and valley dependent.

B. Valley and spin Hall conductivities

In this section, we systematically present a detailed analysis of the VHC and SHC, computed numerically using Eqs. (11) and (14).

In the following, we discuss two physically distinct regimes: the TRS-preserving case ($M = 0$) and the TRS-broken case ($M \neq 0$).

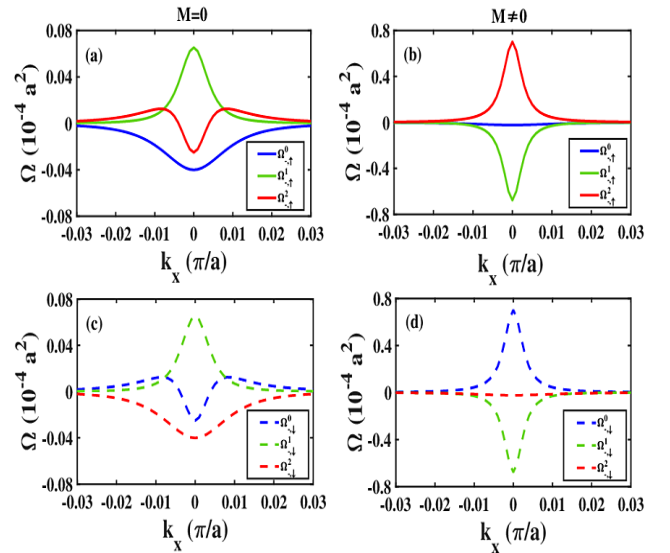


FIG. 4: (Color online) Same as Fig. 3 but for the K' valley.

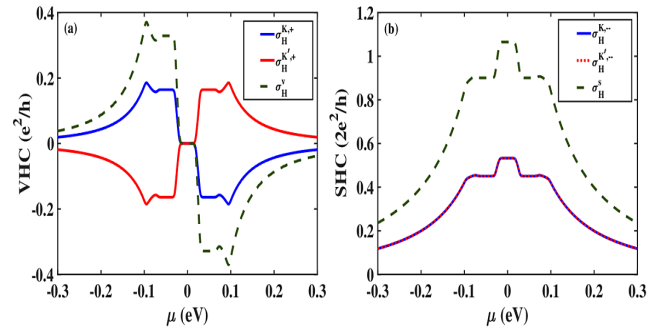


FIG. 5: (Color online) (a) Valley Hall conductivity and (b) Spin Hall conductivity as a function of chemical potential μ for $M = 0$, $\alpha = 0.3$, $T = 20$ K, and $\lambda = 100$ meV.

1. Case I: Hall conductivities in the absence of the staggered magnetization ($M = 0$)

In this case, the anomalous Hall response is solely determined by the Berry curvature generated by the SOI. In Fig. 5(a), we show the variation of the Hall conductivity for a given valley summed over the spin index, i.e., $\sigma_{\text{H}}^{\eta,+} = \sigma_{\text{H}}^{\eta,\uparrow} + \sigma_{\text{H}}^{\eta,\downarrow}$, along with the VHC, as functions of the chemical potential μ , considering $\alpha = 0.3$. The spin integrated AHC in the K valley has the same magnitude but opposite sign compared to that in the K' valley due to the TRS. Therefore, the total AHC vanishes. However, a pure VHC, i.e., $\sigma_{\text{H}}^{\text{v}} = \sigma_{\text{H}}^{K,+} - \sigma_{\text{H}}^{K',+}$ persists, as shown by the dashed line in Fig. 5(a). In addition, the VHC changes sign upon reversal of the chemical potential, demonstrating antisymmetry in μ . Figure 5(b) shows the SHC as a function of μ . For a given valley η , the SHC is defined as $\sigma_{\text{H}}^{\eta,-} = \sigma_{\text{H}}^{\eta,\uparrow} - \sigma_{\text{H}}^{\eta,\downarrow}$, while the total SHC is given by $\sigma_{\text{H}}^{\text{s}} = \sigma_{\text{H}}^{K,-} + \sigma_{\text{H}}^{K',-}$. The SHC contributions from the K and

K' valleys are identical, leading to a nonvanishing total SHC. Unlike the VHC, the SHC remains invariant under the transformation $\mu \rightarrow -\mu$. Both the VHC and SHC display plateau structures in three distinct ranges of μ , which can be identified as SOI induced energy gaps.

To clarify the plateau structure in the VHC, we show the chemical potential dependence of the spin summed AHC in the K valley at $\alpha = 0.3$ in Fig. 6(a). It is evident that $\sigma_{\text{H}}^{K,+}$ attains a plateau whenever μ falls in one of SOI induced gaps (Δ_1 , Δ_2 , and Δ_3) in the band structure, as shown in Fig. 6(b). In the $T \rightarrow 0$ limit, the spin- and valley-resolved AHC given in Eq. (11) becomes

$$\sigma_{\text{H}}^{\eta,\sigma} = \frac{e^2}{h} \sum_{n \in \text{occ}} \int \frac{d^2\mathbf{k}}{2\pi} \Omega_{\eta,\sigma}^n(\mathbf{k}) = \frac{e^2}{h} \sum_{n \in \text{occ}} C_{\eta,\sigma}^{(n)}, \quad (19)$$

where $C_{\eta,\sigma}^{(n)}$ is the spin- and valley-resolved Chern number associated with the n^{th} occupied band. An explicit calculation yields [85] $C_{K,\uparrow}^{(2)} = 0.581$, $C_{K,\downarrow}^{(2)} = -0.416$ and $C_{K,\uparrow}^{(1)} = C_{K,\downarrow}^{(1)} = -0.165$ for $\alpha = 0.3$. The TRS further dictates that $C_{K,\uparrow}^{(n)} = -C_{K',\downarrow}^{(n)}$ and $C_{K,\downarrow}^{(n)} = -C_{K',\uparrow}^{(n)}$. Now the behavior of the spin integrated AHC in the K valley, i.e., $\sigma_{\text{H}}^{K,+}$, can be understood from the following equation:

$$\sigma_{\text{H}}^{K,+} = \frac{e^2}{h} \sum_{n \in \text{occ}} (C_{K,\uparrow}^{(n)} + C_{K,\downarrow}^{(n)}). \quad (20)$$

As μ scans the entire energy spectrum, $\sigma_{\text{H}}^{K,+}$ increases monotonically until μ reaches the top of the spin-up VB. This increase arises because the Berry curvature of the spin-up VB is positive for all \mathbf{k} -values, and the corresponding Chern number is also positive. As μ is increased further (shaded yellow region), $\sigma_{\text{H}}^{K,+}$ begins to decrease since the spin-down VB starts contributing. The Berry curvature of this band is negative for most \mathbf{k} values, which is reflected in its negative Chern number. When μ lies within the gap Δ_1 , $\sigma_{\text{H}}^{K,+}$ attains a plateau. In this regime, both spin-up and spin-down VBs are fully occupied. Consequently, $C_{K,\uparrow}^{(2)} + C_{K,\downarrow}^{(2)} = 0.165$. According to Eq. (20), this yields $\sigma_{\text{H}}^{K,+} = 0.165 e^2/h$. As μ enters a narrow shaded (grey) region, the spin-down FB begins to be occupied. Since its Berry curvature is predominantly negative over almost entire \mathbf{k} values (corresponding to a negative Chern number), $\sigma_{\text{H}}^{K,+}$ decreases sharply and settles into another plateau once μ reaches the gap Δ_2 . When μ is in Δ_2 , the sub-bands $\varepsilon_{K,\uparrow}^{(2)}$, $\varepsilon_{K,\downarrow}^{(2)}$, and $\varepsilon_{K,\downarrow}^{(1)}$ are fully occupied. Hence, Eq. (20) dictates that $\sigma_{\text{H}}^{K,+} = 0$, since $C_{K,\uparrow}^{(2)} + C_{K,\downarrow}^{(2)} + C_{K,\downarrow}^{(1)} = 0$. Upon further increasing μ , $\sigma_{\text{H}}^{K,+}$ exhibits another sharp decrease as the spin-up FB starts to be populated. The Berry curvature of this band is identical to that of the spin-down FB, and consequently it carries the same Chern number. When μ enters the gap $\Delta_3 = \Delta_1$, $\sigma_{\text{H}}^{K,+}$ again attains a plateau. In this regime, all sub-bands of the VB and FB are fully occupied. The height of this plateau is solely determined by the Chern number of the spin-up FB, yielding $\sigma_{\text{H}}^{K,+} = -0.165 e^2/h$. As

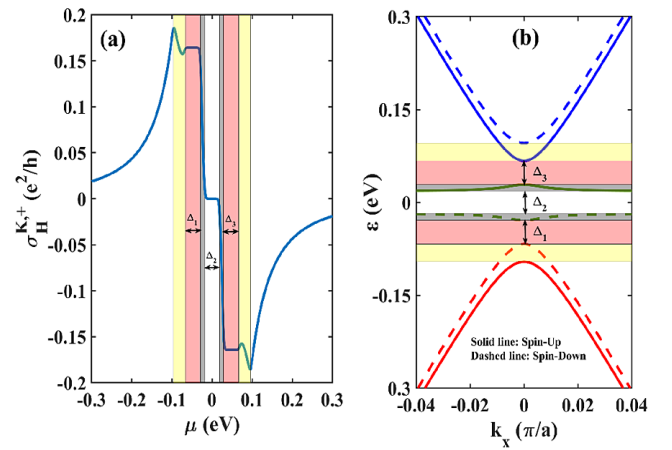


FIG. 6: (a) Spin summed AHC for the K valley at $T = 20$ K and (b) Corresponding low-energy band structure for $\alpha = 0.3$ highlighting the band gaps $\Delta_1 = 38$ meV, $\Delta_2 = 40$ meV, and $\Delta_3 = \Delta_1$. Here, we consider $\lambda = 100$ meV and $M = 0$.

μ is increased further, a similar sequence repeats, with the CB playing the role previously taken by the VB. The behavior of the VHC [Fig. 5(a)] and SHC [Fig. 5(b)] can be understood along the same lines as that of $\sigma_{\text{H}}^{K,+}$.

In Fig. 7(a) and 7(b), we show the chemical potential dependence of the VHC and SHC, respectively, for different values of α . As evident from Fig. 7(a), the VHC vanishes for $\alpha = 0$ and $\alpha = 1$, as a combined effect of TRS and IS. For an intermediate value of α ($0 < \alpha < 1$), a finite valley Hall response emerges as a consequence of broken IS. The behavior of the VHC for $\alpha = 0.3$ has already been discussed in the previous paragraph. For $\alpha = 0.7$, the VHC exhibits similar plateau-like characteristics to those observed for $\alpha = 0.3$, and thus the overall explanation remains the same. However, a striking difference is observed: the plateaus appearing in the gap Δ_1 and Δ_3 have opposite signs for $\alpha = 0.3$ and $\alpha = 0.7$. More specifically, the heights of the plateau in both Δ_1 and Δ_3 undergo a sign change across $\alpha = 0.5$, indicating the occurrence of a TPT, as confirmed in recent studies [84, 85]. Furthermore, the widths of the plateaus vary for different values of α because the spin-orbit gaps are α -dependent.

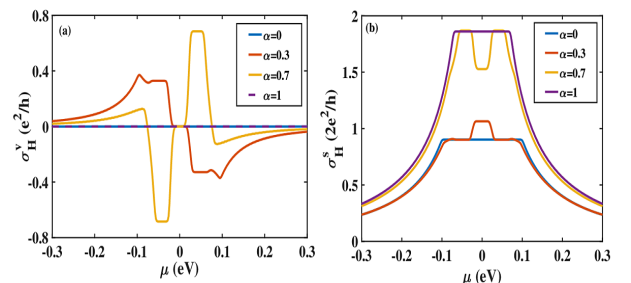


FIG. 7: (Color online) Dependence of the (a) Valley Hall conductivity and (b) Spin Hall conductivity on μ for several α values at $M = 0$.

On the other hand, the SHC for $\alpha = 0$ ($\alpha = 1$) exhibits a smooth plateau $\sigma_H^s \sim 2e^2/h$ ($4e^2/h$), when μ lies within the band gap. For $\alpha = 0$, the FB is absent, and only a single energy gap exists between the CB and the VB, which gives rise to the quantized plateau. For $\alpha = 1$, although the FB is present, it remains undistorted by the SOI. In this case, two gaps appear in the spectrum: one between the CB and FB and another between the FB and VB. These gaps are not separated but share a common boundary through the FB. The presence of these gap regions in the spectrum leads to the wide and smooth SHC plateau observed in these limits. The SHC exhibits three distinct plateaus for $0 < \alpha < 1$, as the SOI opens three well-separated energy gaps, Δ_1 , Δ_2 , and Δ_3 . The plateau height in Δ_1 (as well as in Δ_3) undergoes an abrupt jump from $2e^2/h$ to $4e^2/h$ across $\alpha = 0.5$, consistent with the corresponding change in the spin Chern number from $C_s = 1$ to $C_s = 2$, thereby confirming the occurrence of a TPT.

2. Case II: Hall Conductivities in the Presence of Magnetization ($M \neq 0$)

Here, we discuss the characteristics of the Hall conductivities in the presence of a staggered magnetization $M \neq 0$. As observed earlier, the magnetization modifies the magnitudes and positions of the energy gaps. It also redistributes the Berry curvature around the valleys, thereby significantly influencing the transport responses.

Figures 8(a) and 8(b) show the VHC and SHC as a function of the chemical potential μ for $\alpha = 0.3$ and $M = 50$ meV. Due to the breaking of the TRS, the K and K' valleys contribute differently to the VHC and SHC. In particular, their chemical potential dependences become markedly distinct. While the behavior of $\sigma_H^{K,+}$ remains similar to the corresponding case with $M = 0$, $\sigma_H^{K',+}$ deviates significantly from its nonmagnetic counterpart. A similar distinction is also present between $\sigma_H^{K,-}$ and $\sigma_H^{K',-}$. According to Fig. 2(c) and 2(d) the gap between spin-up VB and spin-up FB in the K' valley becomes much narrower compared to that in the K valley. A similar reduction occurs for the gap between the spin-down CB and spin-down FB. In contrast, the gap between the spin-up FB and spin-down FB in the K' valley becomes significantly wider than that in the K valley, leading to the appearance of a wide central plateau in $\sigma_H^{K',+(-)}$. In addition, the positions of the band gaps are shifted between the two valleys, which causes the plateaus to occur over different ranges of μ in the K and K' valleys. Overall, these features explain the plateau structures observed in σ_H^v and σ_H^s . Notably, a finite anomalous Hall response persists in addition to the spin and valley Hall responses.

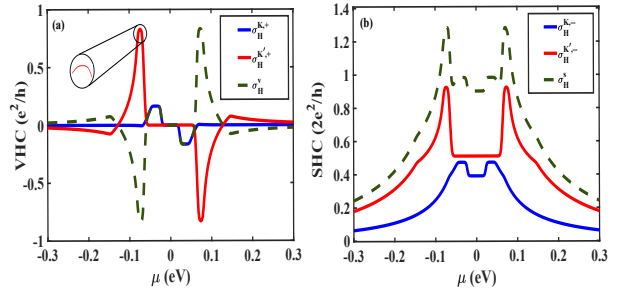


FIG. 8: (Color online) (a) Valley Hall conductivity and (b) Spin Hall conductivity for $\alpha = 0.3$ as a function of chemical potential μ with $M = 50$ meV. The plateau in $\sigma_H^{K',+}$, which apparently appears as a peak, is shown in the zoomed portion.

Figures 9(a) and 9(b) illustrate the μ -dependence of the VHC and SHC, respectively, for different α . For $\alpha = 0$ and $\alpha = 1$, IS is preserved, and hence the VHC vanishes despite the breaking of TRS. However, for $0 < \alpha < 1$, broken IS leads to a finite VHC, which differs significantly from that of the corresponding nonmagnetic case, both in character and magnitude. On the other hand, the SHC for $\alpha = 0$ and $\alpha = 1$ exhibits quantized values e^2/h and $2e^2/h$, respectively, when the chemical potential lies in the energy gap, similar to the $M = 0$ case. This indicates that the system remains in QSH phases with $C_s = 1$ and $C_s = 2$ respectively, even in the presence of finite M . However, this is not the case for $0 < \alpha < 1$, where the interplay between M and α gives rise to a rich topological phase diagram [84], as mentioned earlier. For the chosen values of M and λ , two QSH phases with $C_s = 1$ and $C_s = 2$ are separated by a Quantum spin quantum anomalous Hall phase (QSQAH) with $C = 1$ and $C_s = 3/2$. For a given value of M , the phase boundaries are determined by the critical values of α given by [85]

$$\alpha_{\pm} = \frac{2 \pm \sqrt{5m^2 - m^4}}{4 - m^2}, \quad (21)$$

where $m = M/\lambda$. For our chosen parameters, $M = 50$ meV and $\lambda = 100$ meV, i.e., $m = 1/2$, which yields $\alpha_- \approx 0.24$ and $\alpha_+ \approx 0.82$. Therefore, the considered values of α in Figs. 9(a) and 9(b), i.e., $\alpha = 0.3$ and $\alpha = 0.7$ correspond to the QSQAH phase. Consequently, the corresponding spin and valley Hall responses differ significantly from those of the pure QSH phases.

In the $T \rightarrow 0$ limits, it is possible to determine the analytical expression for the AHC in the $\alpha = 0$ and $\alpha = 1$ limits. When the chemical potential μ lies in the VB(CB), we find for $\alpha = 1$

$$\sigma_H^{\eta,\sigma} = +(-)\eta \frac{e^2}{h} \left[\text{sgn}(\Delta_d) - \frac{\Delta_d}{\sqrt{(\mu^2 + \Delta_d^2)}} \right]. \quad (22)$$

Similarly, for the $\alpha = 0$ case, the AHC is obtained as

$$\sigma_H^{\eta,\sigma} = +(-)\eta \frac{e^2}{2h} \left[\text{sgn}(\Delta_g) - \frac{\Delta_g}{\sqrt{(\mu^2 + \Delta_g^2)}} \right]. \quad (23)$$

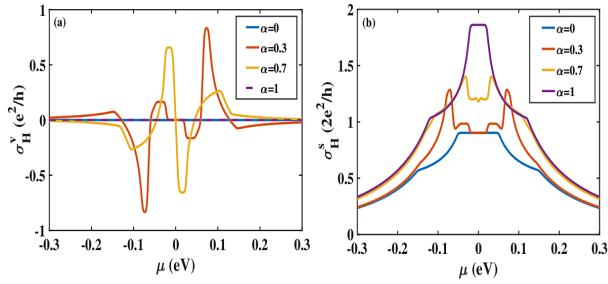


FIG. 9: (Color online) Dependence of the (a) Valley Hall conductivity and (b) Spin Hall conductivity on μ for several α values at $M = 50$ meV.

Using Eqs. (22) and (23), it is straightforward to show that the VHC vanishes in the limiting cases, i.e., $\alpha = 0$ and $\alpha = 1$.

C. Valley and spin Nernst conductivities

In this section, we present a thorough analysis of the Nernst responses of the system in the absence and presence of the staggered magnetization. The VNC and SNC are calculated numerically using Eqs. (12) and (15). In the following, we discuss the characteristic features of the VNC and SNC separately in the two physically distinct regimes: the time-reversal-symmetric case ($M = 0$) and the time-reversal-broken case ($M \neq 0$).

1. Case I: Nernst Conductivities in the absence of Magnetization ($M = 0$)

Figure 10(a) depicts the chemical potential dependence of the spin-summed ANC in individual valleys along with the VNC, while Fig. 10(b) shows the SNC at individual valleys and the total SNC, considering $\alpha = 0.3$. The VNC and SNC are explicitly given by $\alpha_N^V = \alpha_N^{K,+} - \alpha_N^{K',+}$ and $\alpha_N^S = \alpha_N^{K,-} + \alpha_N^{K',-}$, respectively, where $\alpha_N^{\eta,\pm} = \alpha_N^{\eta,\uparrow} \pm \alpha_N^{\eta,\downarrow}$ for $\eta = K, K'$. The VNC contributions from the K and K' valleys are equal in magnitude but opposite in sign due to the TRS, resulting in a vanishing total ANC (both spin and valley integrated). Nevertheless, a finite VNC would persist as shown by the dashed line in Fig. 10 (a). The VNC also appears to be a symmetric function of μ , unlike the VHC. On the other hand, the SNC is valley-degenerate. Therefore, the total SNC (summed over the valley indices) is doubled. In contrast to the VNC, the SNC varies antisymmetrically with the chemical potential. Despite their key differences, both the VNC and SNC exhibit similar features, namely pronounced peak-dip structures and intermediate zero-value plateaus.

To understand the peak-dip features of the VNC and SNC, we replot $\alpha_N^{K,+}$ in Fig. 11(a), with the various regions of the spectrum indicated by shaded areas. The zero-value plateau regions of $\alpha_N^{K,+}$ correspond to the SOI-induced band gaps Δ_1 , Δ_2 , and Δ_3 . Generally, the characteristic features of the

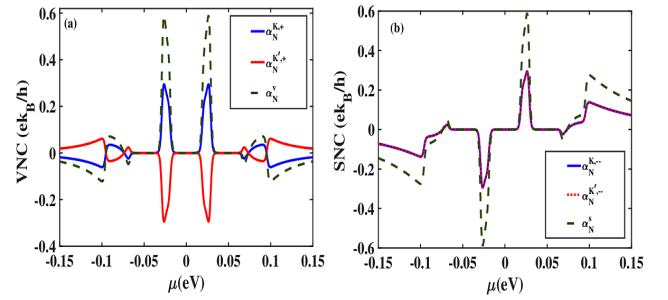


FIG. 10: (Color online) (a) Valley Nernst conductivity and (b) Spin Nernst conductivity as a function of chemical potential μ for $\alpha = 0.3$ and $M = 0$.

ANC are mainly governed by the interplay between the Berry curvature and the entropy density. The entropy density function $S_{\eta,\sigma}^n(\mathbf{k})$, which enters directly in Eq. (12), depends solely on the Fermi-Dirac distribution function f . At low temperatures, it shows a typical step-like profile and vanishes for fully occupied ($f = 1$) or empty states ($f = 0$). At half filling ($f = 1/2$), it reaches a maximal value of $\ln 2$, evident from Eq. (13). The variation of the entropy density with μ is shown in Fig. 11(b). When μ approaches a band edge, the entropy density becomes sharply peaked within an energy window of the order of a few $k_B T$. The overlap of the entropy density with the Berry curvature hotspots near band extrema provides the key mechanism responsible for the peak-dip structures in $\alpha_N^{K,+}$. For instance, $\alpha_N^{K,+}$ decreases monotonically as μ approaches the top of the spin-up VB [Region I in Fig. 11 (a)]. This occurs because the entropy density increases and the Berry curvature is positive for all \mathbf{k} , with a peak at $\mathbf{k} = 0$. As μ crosses the spin-up VB $\alpha_N^{K,+}$ undergoes a sign change from $-$ to $+$. At this point, states from the spin-down VB begin to contribute, whose Berry curvature is negative over certain regions of \mathbf{k} space and dominates over the contribution from the spin-up VB. Consequently, $\alpha_N^{K,+}$ decreases within the shaded (yellow) region II and attains a dip when μ reaches the top of the spin-down VB. This behavior results from the combined effect of the Berry curvature of the VBs and the entropy density. When μ lies within the band gap Δ_1 (region III), $\alpha_N^{K,+}$ vanishes because the entropy density becomes zero in the gap, as evident from Fig. 11(b). The small deviation from zero near the edges of Δ_1 arises from finite-temperature effects. As μ enters the shaded gray region IV, $\alpha_N^{K,+}$ exhibits a large peak whose width is of the order of that region. In this regime, the states of the spin-down VB become occupied; their Berry curvature is negative for all \mathbf{k} and exhibits a pronounced dip at $\mathbf{k} = 0$. Although the entropy density decreases across this region, it remains positive, which leads to the observed peak in $\alpha_N^{K,+}$. When μ enters the gap Δ_2 (region V), $\alpha_N^{K,+}$ again exhibits a zero-value plateau due to the vanishing entropy density $S_{\eta,\sigma}^n$. For $\mu > 0$ (regions VI-IX), the same behavior repeats with the role of the VBs replaced by that of the CBs. The explanations of the peak-dip structures in the VNC and SNC follow the same reasoning as in the case of

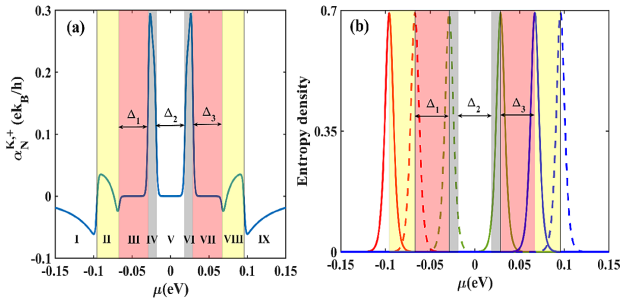
$\alpha_N^{K,+}$


FIG. 11: (Color online) (a) Spin summed ANC in the K valley and (b) corresponding entropy density for $\alpha = 0.3$.

Sharp peak-dip features in panel (a) coincide with the entropy maxima in panel (b) and occur near band edges, where the Berry curvature is strongly enhanced. The shaded regions III, V, and VII denote the band gaps in which both entropy and $\alpha_N^{K,+}$ are suppressed.

The behavior of the Nernst conductivities shown in Fig. 10 can also be understood from the Mott relation, which connects the thermoelectric and electrical Hall responses. At low temperature, the Nernst conductivity α_{xy} is proportional to the energy derivative of the Hall conductivity σ_{xy} ,

$$\alpha_{xy} = -\frac{\pi^2 k_B^2 T}{3e} \left. \frac{d\sigma_{xy}}{d\mu} \right|_{\mu=E_F}. \quad (24)$$

Comparing Figs. 6(a) and 11(a), it is clear that $\alpha_N^{K,+}$ is proportional to the negative derivative of $\sigma_H^{K,+}$ with respect to the chemical potential μ , which naturally explains the entire structure of $\alpha_N^{K,+}$, including the peak-dip features, plateau regions, and the sign changes near the band edges, as discussed in the following. In regions where $\sigma_H^{K,+}$ is nearly constant as a function of μ , its derivative is close to zero, resulting in the plateau-like behavior of $\alpha_N^{K,+}$. When $\sigma_H^{K,+}$ varies rapidly with μ , the magnitude of its derivative becomes large, leading to pronounced peak-dip structures in $\alpha_N^{K,+}$. Because of the negative proportionality, the sign of $\alpha_N^{K,+}$ is opposite to the slope of $\sigma_H^{K,+}$ that means a positive(negative) slope of $\sigma_H^{K,+}$ produces a negative(positive) contribution to $\alpha_N^{K,+}$. Accordingly, at the band edges, where the slope of $\sigma_H^{K,+}$ reverses, $\alpha_N^{K,+}$ undergoes a sign change.

The variation of the VNC and SNC with μ for different values of α are shown in Figs. 12(a) and 12(b), respectively. The simultaneous presence of TRS and IS enforces a vanishing VNC for $\alpha = 0$ and $\alpha = 1$, due to $S_{\eta,\uparrow}^n = S_{\eta,\downarrow}^n$ and $\Omega_{\eta,\uparrow}^n = -\Omega_{\eta,\downarrow}^n$. A finite VNC appears for $0 < \alpha < 1$ owing to broken IS. The peak-dip features of VNC for $\alpha = 0.3$ and $\alpha = 0.7$ are completely different. It is verified (not shown here) that all the major peaks/dips undergo a sign change across $\alpha = 0.5$. This may be considered as an indication of TPT. On the other hand, the SNC exhibits wide zero-value plateaus for $\alpha = 0$ and $\alpha = 1$. Similar to the VNC, the peaks and dips in the

SNC for $0 < \alpha < 1$ would also display a sign change across $\alpha = 0.5$.

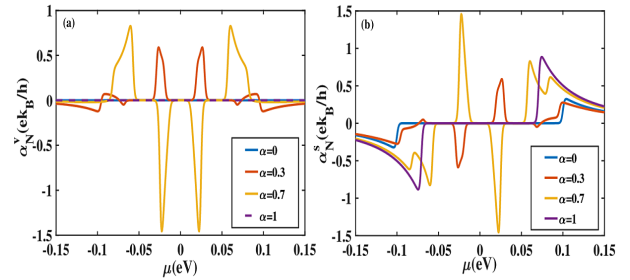


FIG. 12: (Color online) Dependence of the (a) Valley Nernst conductivity and (b) Spin Nernst conductivity on μ for several α values at $M = 0$.

2. Nernst Conductivities in the Presence of Magnetization ($M \neq 0$)

The presence of a staggered magnetization leads to a drastic change in the Nernst response of the system as shown in Fig. 13. As shown in Fig. 13, K and K' valleys contribute differently due to breaking of the TRS. The peak-dip feature of $\alpha_N^{K,+}$ is more prominent than that of $\alpha_N^{K',+}$, thus leading to a nonvanishing total ANC (not shown) in addition to the finite VNC (dashed line). Figure 13(b) shows that SNCs at individual valleys are completely different. In fact the total SNC is dominated by the contribution from the K' valley.

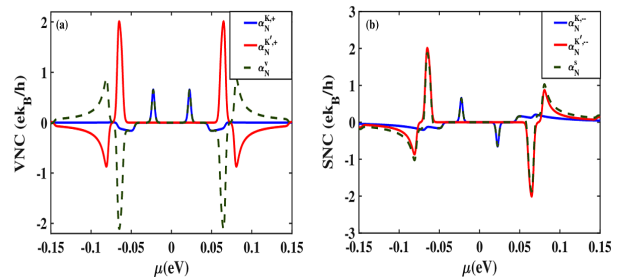


FIG. 13: (Color online) (a) Valley Nernst conductivity and (b) Spin Nernst conductivity as a function of chemical potential μ with $\alpha = 0.3$ and $M = 50$ meV.

The dependence of the VNC and SNC on the chemical potential for various values of α are depicted in Figs. 14(a) and 14(b), respectively. The VNC disappears for $\alpha = 0$ and $\alpha = 1$ due to IS. In contrast, the SNC remains finite and exhibits characteristic features in these limits. The other values of α , namely $\alpha = 0.3$ and $\alpha = 0.7$ considered in Figs. 14(a) and 14(b) correspond to the QSQS phase with $C = 1$ and $C_s = 3/2$ for the chosen value of M . Figs. 14(a) and 14(b) further confirm that the spin-valley Nernst responses in this mixed phase strongly depend on α .

At low temperatures, using Eq. (12), we obtain analytical expressions for the ANC in the $\alpha = 0$ and $\alpha = 1$ limits. The

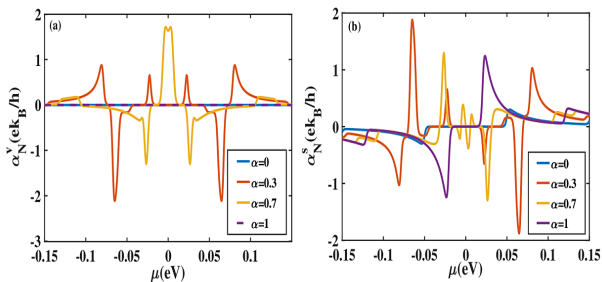


FIG. 14: (Color online) Dependence of the (a) Valley Nernst conductivity and (b) Spin Nernst conductivity on μ for several α values considering $M = 50$ meV.

ANC takes a non-zero value when the chemical potential μ lies within the band and vanishes otherwise. For $\alpha = 1$, when the chemical potential μ lies in the CB(VB), we obtain the simpler form of the ANC as

$$\alpha_N^{\eta,\sigma} = +(-)\eta \frac{\pi k_B e T \Delta_d}{6h\mu^2} \quad (25)$$

and similarly for $\alpha = 0$, the ANC is obtained as

$$\alpha_N^{\eta,\sigma} = +(-)\eta \frac{\pi k_B e T \Delta_g}{12h\mu^2}. \quad (26)$$

D. Spin and Valley Polarization

In this section, we examine the spin and valley polarization calculated from the Nernst conductivities in the presence of a staggered magnetization. We have calculated the spin and valley polarizations analytically for $\alpha = 0$ and $\alpha = 1$ limits and numerically for $0 < \alpha < 1$. For $\alpha = 0$ and $\alpha = 1$ limits, the IS is preserved, resulting in a spin degeneracy of the states. Consequently, in these limits, the spin polarization vanishes. However, due to the breaking of TRS by staggered magnetization, the valley degeneracy is lifted, leading to a non-zero valley polarization.

For $\alpha = 1$, using Eq. (16) and assuming that the chemical potential μ lies in the VB, the valley polarization is obtained as

$$P_v = -\frac{\sqrt{2}M}{\lambda}, \quad \text{for } \lambda > \sqrt{2}M, \quad (27)$$

where the SOI dominates over the staggered magnetization.

When the staggered magnetization exceeds the value $\lambda/\sqrt{2}$, we obtain

$$P_v = -\frac{\lambda}{\sqrt{2}M}, \quad \text{for } \lambda < \sqrt{2}M. \quad (28)$$

Similarly, for $\alpha = 0$, the valley polarization becomes

$$P_v = -\frac{M}{\lambda}, \quad \text{for } \lambda > M, \quad (29)$$

and

$$P_v = -\frac{\lambda}{M}, \quad \text{for } \lambda < M. \quad (30)$$

For both $\alpha = 1$ and $\alpha = 0$ limits, in the SOI-dominated regime, P_v increases linearly with the staggered magnetization. However, in the magnetization-dominated regime, P_v decreases inversely with the staggered magnetization.

Compared to the $\alpha = 1$ case, the magnitude of the valley polarization in the $\alpha = 0$ limit is reduced by a factor of $\sqrt{2}$ for the SOI-dominated regime and increased by a factor of $\sqrt{2}$ for the magnetization-dominated regime.

The contour plot of the spin polarization P_s for $\alpha = 0.3$ is shown in Fig. 15(a). The spin polarization shows strong dependence on both the chemical potential μ and the parameter M/λ . Over a wide range of the parameter, $|P_s|$ is close to unity, indicating that a single spin channel dominates the Nernst response. It is observed that the polarization is anti-symmetric with respect to $\mu = 0$. In particular, for $\mu < 0$, P_s is mostly positive, while for $\mu > 0$ it is mainly negative. Figure 15(b) shows the corresponding results for $\alpha = 0.7$. In contrast to the $\alpha = 0.3$ case, the spin polarization now shows a more mixed behavior. The clear separation between spin-dominated regions observed at $\alpha = 0.3$ is no longer present. Instead, both positive and negative spin-polarization appear on each side of $\mu = 0$. The coexistence of opposite spin polarizations on the same side of $\mu = 0$ signals strong competition between spin channels.

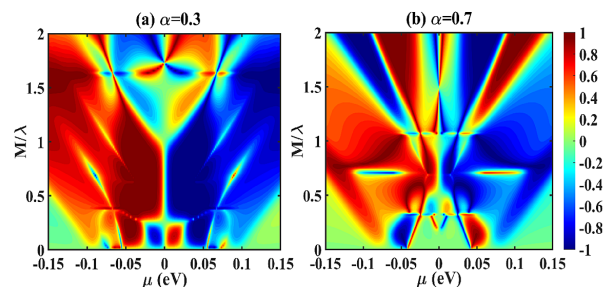


FIG. 15: (Color online) Contour plot of the spin polarization for (a) $\alpha = 0.3$ and (b) $\alpha = 0.7$.

Figure 16(a) shows the contour plot of the valley polarization P_v at $\alpha = 0.3$. Unlike the spin polarization, the valley polarization shows significantly different features. It is symmetric about $\mu = 0$. The most prominent feature is the emergence of an extended region with $P_v \approx 1$ over a wide range of the parameter values. This indicates a strong imbalance between the thermoelectric contributions originating from the K and K' valleys. The corresponding result for $\alpha = 0.7$ is illustrated in Fig. 16(b). Compared to the $\alpha = 0.3$ case, the P_v for $\alpha = 0.7$ occupies a larger portion of the $(\mu, M/\lambda)$ plane. It can be seen that P_v remains close to unity over a wide range of the parameter values, indicating a strong valley selectivity where the contribution from the K' valley is strongly suppressed. Importantly, the P_v shows robust feature as it remains nearly

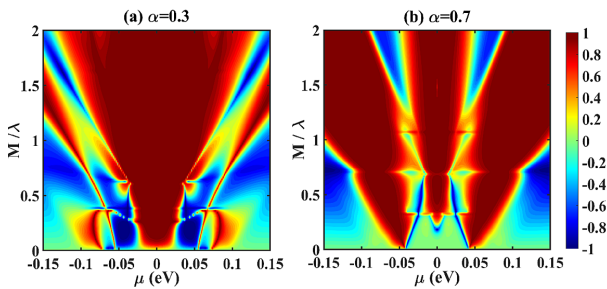


FIG. 16: (Color online) Contour plot of the valley polarization for (a) $\alpha = 0.3$ and (b) $\alpha = 0.7$.

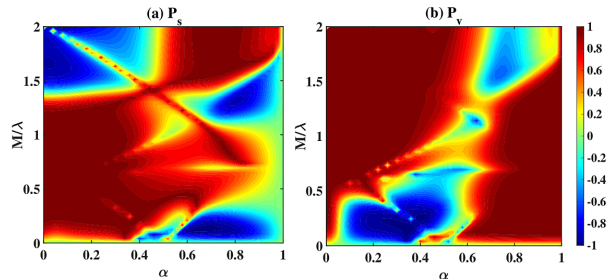


FIG. 17: (Color online) Contour plot of (a) Spin polarization and (b) Valley polarization. We fix the chemical potential to $\mu = -50$ meV.

saturated for almost the entire range of the parameter value near $\mu = 0$, reflecting the strong valley asymmetry induced by the magnetization.

In Fig. 17, we present the spin and valley polarizations over the entire range of α , with the chemical potential fixed to $\mu = -50$ meV. As shown in Fig. 17(a), there exist extended regions in the $(\alpha, M/\lambda)$ plane where $P_s \approx 1$, indicating a strong dominance of the spin-up channel. There are a few small regions where $P_s \approx -1$. Similarly, P_v approaches unity over broad parameter ranges in the $(\alpha, M/\lambda)$ plane, implying that the K valley predominantly contributes to the valley polarization [see Fig. 17(b)]. In addition, a few localized

hotspots appear where the K' valley becomes the dominant contributor.

V. SUMMARY

We have presented a comprehensive study of the spin- and valley-resolved anomalous Hall and Nernst effects in the spin-orbit coupled α - T_3 system. By incorporating the Kane–Mele type SOI and staggered sublattice magnetization into the model, we have shown that the Berry curvature and entropy-weighted transport coefficients are highly tunable. In the TRS-preserving regime, the system exhibits a pure valley Hall effect accompanied by a robust spin Hall response. The corresponding Nernst conductivities display characteristic peak–dip structures governed by the entropy-weighted Berry curvature distribution near the band edges. For intermediate α values, these curvatures become sharply localized, resulting in enhanced Hall and Nernst signals. When TRS is broken by the staggered magnetization, the transport behavior changes significantly. Valley degeneracy is lifted, producing strong asymmetries between the K and K' valleys. The Berry curvature reorganizes into highly valley-polarized hotspots, generating large anomalous Hall and Nernst effects with tunable sign and magnitude. The strongest responses emerge at intermediate α values, where the interplay of flat band physics and staggered magnetization-induced band modification is most pronounced. We have also shown that the Nernst response of the α - T_3 system can generate strong spin and valley polarizations, with a high degree of tunability controlled by the parameters μ , M , λ , and α . Both the spin and valley polarizations exhibit rich structures, with extended regions of complete polarization. Overall, our results establish that Berry-curvature driven anomalous thermoelectric effects in the α - T_3 system provide an efficient route to generate and control spin- and valley-polarized currents. The strong and tunable polarization demonstrated here suggests promising opportunities for spin- and valley-caloritronic device applications.

-
- [1] S. A Wolf, D. D. Awschalom, R. A. Buhrman, J. M. Daughton, S. Von Molnar, M. L. Roukes, A. Y. Chtchelkanova, and D. M. Treger, Spintronics: A Spin- Based Electronics Vision for the Future, *Science* **294**, 1488 (2001).
 - [2] I. Zutic, J. Fabian, and S. Das Sarma, Spintronics: Fundamentals and applications, *Rev. Mod. Phys.* **76**, 323 (2004).
 - [3] D. D. Awschalom and M. E. Flatte, Challenges for semiconductor spintronics, *Nat. Phys.* **3**, 153 (2007).
 - [4] A. Fert, Nobel Lecture: Origin, development, and future of spintronics, *Rev. Mod. Phys.* **80**, 1517 (2008).
 - [5] D. D. Awschalom and N. Samarth, Spintronics without magnetism, *Physics* **2**, 50 (2009).
 - [6] A. Aharony, O. Entin-Wohlman, Y. Tokura, and S. Katsumoto, Spin filtering by a periodic spintronic device, *Phys. Rev. B* **78**, 125328 (2008).
 - [7] Z. G. Zhu, Selective spin injection controlled by electrical way in ferromagnet/quantum dot/semiconductor system, *Phys. Lett. A* **372**, 695 (2008).
 - [8] J. E. Hirsch, Spin Hall Effect, *Phys. Rev. Lett.* **83**, 1834 (1999).
 - [9] E. G. Mishchenko, A. V. Shytov, and B. I. Halperin, Spin Current and Polarization in Impure Two-Dimensional Electron Systems with Spin-Orbit Coupling, *Phys. Rev. Lett.* **93**, 226602 (2004).
 - [10] R. Raimondi, C. Gorini, M. Dzierzawa, and P. Schwab, Current-induced spin polarization and the spin Hall effect: A quasiclassical approach, *Solid State Commun.* **144**, 524 (2007).
 - [11] S. D. Ganichev, E. L. Ivchenko, V. V. Bel'kov, S. A. Tarasenko, M. Sollinger, D. Weiss, W. Wegscheider, and W. Prettl, Spin-galvanic effect, *Nature* **417**, 153 (2002).
 - [12] M. J. Stevens, A. L. Smirl, R. D. R. Bhat, A. Najmaie, J. E. Sipe,

- and H. M. van Driel, Quantum Interference Control of Ballistic Pure Spin Currents in Semiconductors, *Phys. Rev. Lett.* **90**, 136603 (2003).
- [13] J. Hübner, W. W. Rühle, M. Klude, D. Hommel, R. D. R. Bhat, J. E. Sipe, and H. M. van Driel, Direct Observation of Optically Injected Spin-Polarized Currents in Semiconductors, *Phys. Rev. Lett.* **90**, 216601 (2003).
- [14] Z. Ma, R. L. Wu, Y. B. Yu, and M. Wang, Voltage-controllable generator of pure spin current: A three-terminal model, *J. Appl. Phys.* **116**, 043706 (2014).
- [15] S. Datta and B. Das, Electronic analog of the electro-optic modulator, *Appl. Phys. Lett.* **56**, 665 (1990).
- [16] S. Gardelis, C. G. Smith, C. H. W. Barnes, E. H. Linfield, and D. A. Ritchie, Spin-valve effects in a semiconductor field-effect transistor: A spintronic device, *Phys. Rev. B* **60**, 7764 (1999).
- [17] G. Schmidt, D. Ferrand, L. W. Molenkamp, A. T. Filip, and B. J. van Wees, Fundamental obstacle for electrical spin injection from a ferromagnetic metal into a diffusive semiconductor, *Phys. Rev. B* **62**, R4790(R) (2000).
- [18] C. M. Hu, J. Nitta, A. Jensen, J. B. Hansen, and H. Takayanagi, Spin-polarized transport in a two-dimensional electron gas with interdigital-ferromagnetic contacts, *Phys. Rev. B* **63**, 125333 (2001).
- [19] N. Tombros, C. Jozsa, M. Popinciuc, H. T. Jonkman, and B. J. V. Wees, Electronic spin transport and spin precession in single graphene layers at room temperature, *Nature* **448**, 571 (2007).
- [20] Q. Zhang, K. S. Chan, and Z. Lin, Spin current generation by adiabatic pumping in monolayer graphene, *Appl. Phys. Lett.* **98**, 032106 (2011).
- [21] S. Souma and M. Ogawa, Pure spin current induced by adiabatic quantum pumping in zigzag-edged graphene nanoribbons, *Appl. Phys. Lett.* **104**, 183103 (2014).
- [22] R. Mohammadkhani, B. Abdollahipour, and M. Alidoust, Strain-controlled spin and charge pumping in graphene devices via spin-orbit coupled barriers, *EPL* **111**, 67005 (2015).
- [23] G. E. W. Bauer, A. H. MacDonald, and S. Maekawa, Spin Caloritronics, *Solid State Commun.* **150**, 459 (2010).
- [24] G. E. W. Bauer, E. Saitoh, and B. J. van Wees, Spin caloritronics, *Nat. Mater.* **11**, 391 (2012).
- [25] K. Uchida, S. Takahashi, K. Harii, J. Ieda, W. Koshibae, K. Ando, S. Maekawa, and E. Saitoh, Observation of the spin Seebeck effect, *Nature* **455**, 778 (2008).
- [26] K. Uchida, J. Xiao, H. Adachi, J. Ohe, S. Takahashi, J. Ieda, T. Ota, Y. Kajiwara, H. Umezawa, H. Kawai, G. E. W. Bauer, S. Maekawa, and E. Saitoh, Spin Seebeck insulator, *Nat. Mater.* **9**, 894 (2010).
- [27] C. M. Jaworski, J. Yang, S. Mack, D. D. Awschalom, J. P. Heremans, and R. C. Myers, Observation of the spin-Seebeck effect in a ferromagnetic semiconductor, *Nat. Mater.* **9**, 898 (2010).
- [28] A. D. Avery, M. R. Pufall, and B. L. Zink, Observation of the Planar Nernst Effect in Permalloy and Nickel Thin Films with In-Plane Thermal Gradients, *Phys. Rev. Lett.* **109**, 196602 (2012).
- [29] S. Y. Huang, W. G. Wang, S. F. Lee, J. Kwo, and C. L. Chien, Intrinsic Spin-Dependent Thermal Transport, *Phys. Rev. Lett.* **107**, 216604 (2011).
- [30] X. Chen, L. Zhang, and H. Guo, Valley caloritronics and its realization by graphene nanoribbons, *Phys. Rev. B* **92**, 155427 (2015).
- [31] D. Xiao, W. Yao, and Q. Niu, Valley-Contrasting Physics in Graphene: Magnetic Moment and Topological Transport, *Phys. Rev. Lett.* **99**, 236809 (2007).
- [32] T. Fujita, M. B. A. Jalil, and S. G. Tan, Valley filter in strain engineered graphene, *Appl. Phys. Lett.* **97**, 043508 (2010).
- [33] W. Yao, D. Xiao, and Q. Niu, Valley-dependent optoelectronics from inversion symmetry breaking, *Phys. Rev. B* **77**, 235406 (2008).
- [34] R. Saxena, A. Saha, and S. Rao, Conductance, valley and spin polarizations, and tunneling magnetoresistance in ferromagnetic-normal-ferromagnetic junctions of silicene, *Phys. Rev. B* **92**, 245412 (2015).
- [35] K. F. Mak, K. L. McGill, J. Park, and P. L. McEuen, The valley Hall effect in MoS₂ transistors, *Science* **344**, 1489 (2014).
- [36] D. Xiao, G.-B. Liu, W. Feng, X. Xu, and W. Yao, Coupled Spin and Valley Physics in Monolayers of MoS₂ and Other Group-VI Dichalcogenides, *Phys. Rev. Lett.* **108**, 196802 (2012).
- [37] T. Jungwirth, Q. Niu, and A. H. MacDonald, Anomalous Hall Effect in Ferromagnetic Semiconductors, *Phys. Rev. Lett.* **88**, 207208 (2002).
- [38] N. Nagaosa, J. Sinova, S. Onoda, A. H. MacDonald, and N. P. Ong, Anomalous Hall Effect, *Rev. Mod. Phys.* **82**, 1539 (2010).
- [39] X.-Q. Yu, Z.-G. Zhu, G. Su, and A.-P. Jauho, Thermally Driven Pure Spin and Valley Currents via the Anomalous Nernst Effect in Monolayer Group-VI Dichalcogenides, *Phys. Rev. Lett.* **115**, 246601 (2015).
- [40] G. Sharma, Tunable topological Nernst effect in two-dimensional transition-metal dichalcogenides, *Phys. Rev. B* **98**, 075416 (2018).
- [41] D. L. Bergman and V. Oganesyan, Theory of Dissipationless Nernst Effects, *Phys. Rev. Lett.* **104**, 0666011 (2010).
- [42] T. Yokoyama and S. Murakami, Transverse magnetic heat transport on the surface of a topological insulator, *Phys. Rev. B* **83**, 161407 (R) (2011).
- [43] D. Xiao, Y. Yao, Z. Fang, and Q. Niu, Berry-Phase Effect in Anomalous Thermoelectric Transport, *Phys. Rev. Lett.* **97**, 026603 (2006).
- [44] M. T. Dau, C. Vergnaud, A. Marty, C. Beigne, S. Gambarelli, V. Maurel, T. Journot, B. Hyot, T. Guillet, B. Grevin, H. Okuno, and M. Jamet, The valley Nernst effect in WSe₂, *Nat. Commun.* **10**, 5796 (2010).
- [45] Z. A. Xu, N. P. Ong, Y. Wang, T. Kakeshita, and S. Uchida, Vortex-like excitations and the onset of superconducting phase fluctuation in underdoped La_{2-x}Sr_xCuO₄, *Nature* **406**, 486 (2000).
- [46] Y. Wang, Z. A. Xu, T. Kakeshita, S. Uchida, S. Ono, Y. Ando, and N. P. Ong, Onset of the vortexlike Nernst signal above T_c in La_{2-x}Sr_xCuO₄ and Bi₂Sr_{2-y}La_yCuO₆, *Phys. Rev. B* **64**, 224519 (2001).
- [47] Y. Onose, Y. Shiomi, and Y. Tokura, Lorenz Number Determination of the Dissipationless Nature of the Anomalous Hall Effect in Itinerant Ferromagnets, *Phys. Rev. Lett.* **100**, 016601 (2008).
- [48] M. Hirschberger, R. Chisnell, Y. S. Lee, and N. P. Ong, Thermal Hall Effect of Spin Excitations in a Kagome Magnet, *Phys. Rev. Lett.* **115**, 106603 (2015).
- [49] H. Doki, M. Akazawa, H.-Y. Lee, J. H. Han, K. Sugii, M. Shimozawa, N. Kawashima, M. Oda, H. Yoshida, and M. Yamashita, Spin Thermal Hall Conductivity of a Kagome Antiferromagnet, *Phys. Rev. Lett.* **121**, 097203 (2018).
- [50] X. Zhou, H. Liu, W. Wu, K. Jiang, Y. Shi, Z. Li, Y. Sui, J. Hu, and J. Luo, Anomalous thermal Hall effect and anomalous Nernst effect of CsV₃Sb₅, *Phys. Rev. B* **105**, 205104 (2022).
- [51] E. Illes, Properties of the α -T₃ model, PhD Thesis, *University of Guelph* (2017).
- [52] B. Sutherland, Localization of electronic wave functions due to local topology, *Phys. Rev. B* **34**, 5208 (1986).
- [53] J. Vidal, R. Mosseri, and B. Douçot, Aharonov-Bohm Cages in Two-Dimensional Structures, *Phys. Rev. Lett.* **81**, 5888 (1998).

- [54] C. C. Abilio, P. Butaud, T. Fournier, B. Pannetier, J. Vidal, S. Tedesco, and B. Dalzotto, Magnetic Field Induced Localization in a Two-Dimensional Superconducting Wire Network, *Phys. Rev. Lett.* **83**, 5102 (1999).
- [55] A. Raoux, M. Morigi, J. N. Fuchs, F. Piechon, and G. Montambaux, From Dia- to Paramagnetic Orbital Susceptibility of Massless Fermions, *Phys. Rev. Lett.* **112**, 026402 (2014).
- [56] E. Illes, J. P. Carbotte, and E. J. Nicol, Hall quantization and optical conductivity evolution with variable Berry phase in the α - T_3 model, *Phys. Rev. B* **92**, 245410 (2015).
- [57] T. Biswas and T. K. Ghosh, Magnetotransport properties of the α - T_3 model, *J. Phys.: Condens. Matter* **28**, 495302 (2016).
- [58] E. Illes and E. J. Nicol, Klein tunneling in the α - T_3 model, *Phys. Rev. B* **95**, 235432 (2017).
- [59] SK. F. Islam and P. Dutta, Valley-polarized magnetoconductivity and particle-hole symmetry breaking in a periodically modulated α - T_3 lattice, *Phys. Rev. B* **96**, 045418 (2017).
- [60] T. Biswas and T. K. Ghosh, Dynamics of a quasiparticle in the α - T_3 model: role of pseudospin polarization and transverse magnetic field on zitterbewegung, *J. Phys.: Condens. Matter* **30**, 075301 (2018).
- [61] A. Balassis, D. Dahal, G. Gumbs, A. Iurov, D. Huang and O. Roslyak, Magnetoplasmons for the α - T_3 model with filled Landau levels, *J. Phys.: Condens. Matter* **32**, 485301 (2020).
- [62] A. Iurov, G. Gumbs, and D. Huang, Many-body effects and optical properties of single and double layer α - T_3 lattices, *J. Phys.: Condens. Matter* **32**, 415303 (2020).
- [63] A. Iurov, L. Zhemchuzhna, G. Gumbs, D. Huang, D. Dahal, and Y. Abranyos, Finite-temperature plasmons, damping, and collective behavior in the α - T_3 model, *Phys. Rev. B* **105**, 245414 (2022).
- [64] E. Illes and E. J. Nicol, Magnetic properties of the α - T_3 model: Magneto-optical conductivity and the Hofstadter butterfly, *Phys. Rev. B* **94**, 125435 (2016).
- [65] A. D. Kovacs, G. David, B. Dora, and J. Cserti, Frequency-dependent magneto-optical conductivity in the generalized α - T_3 model, *Phys. Rev. B* **95**, 035414 (2017).
- [66] Y. R. Chen, Y. Xu, J. Wang, J. F. Liu, and Z. Ma, Enhanced magneto-optical response due to the flat band in nanoribbons made from the α - T_3 lattice, *Phys. Rev. B* **99**, 045420 (2019).
- [67] L. Chen, J. Zuber, Z. Ma, and C. Zhang, Nonlinear optical response of the α - T_3 model due to the nontrivial topology of the band dispersion, *Phys. Rev. B* **100**, 035440 (2019).
- [68] D. O. Oriekhov and V. P. Gusynin, RKKY interaction in a doped pseudospin-1 fermion system at finite temperature, *Phys. Rev. B* **101**, 235162 (2020).
- [69] O. Roslyak, G. Gumbs, A. Balassis, and H. Elsayed, Effect of magnetic field and chemical potential on the RKKY interaction in the α - T_3 lattice, *Phys. Rev. B* **103**, 075418 (2021).
- [70] J. Wang, J. F. Liu, and C. S. Ting, Recovered minimal conductivity in the α - T_3 model, *Phys. Rev. B* **101**, 205420 (2020).
- [71] M. W. Alam, B. Souayah, and SK. F. Islam, Enhancement of thermoelectric performance of a nanoribbon made of α - T_3 lattice, *J. Phys.: Condens. Matter* **31**, 485303 (2019).
- [72] W. Duan, Seebeck and Nernst effects of pseudospin-1 fermions in the α - T_3 model under magnetic fields, *Phys. Rev. B* **108**, 155428 (2023).
- [73] A. Yan, X. Wang, and Y. X. Li, Nernst and seebeck effects in α - T_3 lattice, *J. Phys.: Condens. Matter* **36**, 305705 (2024).
- [74] F. Wang and Y. Ran, Nearly flat band with Chern number $C = 2$ on the dice lattice, *Phys. Rev. B* **84**, 241103(R) (2011).
- [75] D. F. Urban, D. Bercioux, M. Wimmer, and W. Husler, Barrier transmission of Dirac-like pseudospin-one particles, *Phys. Rev. B* **84**, 115136 (2011).
- [76] J. D. Malcolm and E. J. Nicol, Magneto-optics of massless Kane fermions: Role of the flat band and unusual Berry phase, *Phys. Rev. B* **92**, 035118 (2015).
- [77] B. Dey and T. K. Ghosh, Photoinduced valley and electron-hole symmetry breaking in α - T_3 lattice: The role of a variable Berry phase, *Phys. Rev. B* **98**, 075422 (2018).
- [78] B. Dey and T. K. Ghosh, Floquet topological phase transition in the α - T_3 lattice, *Phys. Rev. B* **99**, 205429 (2019).
- [79] A. Iurov, G. Gumbs, and D. Huang, Peculiar electronic states, symmetries, and Berry phases in irradiated α - T_3 materials, *Phys. Rev. B* **99**, 205135 (2019).
- [80] L. Tamang, T. Nag, and T. Biswas, Floquet engineering of low-energy dispersions and dynamical localization in a periodically kicked three-band system, *Phys. Rev. B* **104**, 174308 (2021).
- [81] L. Tamang and T. Biswas, Probing topological signatures in an optically driven α - T_3 lattice, *Phys. Rev. B* **107**, 085408 (2023).
- [82] C. L. Kane and E. J. Mele, Quantum Spin Hall Effect in Graphene, *Phys. Rev. Lett.* **95**, 226801 (2005).
- [83] C. L. Kane and E. J. Mele, Z_2 Topological Order and the Quantum Spin Hall Effect, *Phys. Rev. Lett.* **95**, 146802 (2005).
- [84] J. Wang and J. F. Liu, Quantum spin Hall phase transition in the α - T_3 lattice, *Phys. Rev. B* **103**, 075419 (2021).
- [85] L. Tamang, S. Verma, and T. Biswas, Orbital magnetization senses the topological phase transition in a spin-orbit coupled α - T_3 system, *Phys. Rev. B* **110**, 165426 (2024).